PAPER

Check for updates

Lanthanide-doped Na₂MgScF₇ exhibiting downshifting and upconversion emissions for multicolor anti-counterfeiting†

Chengyu Zhuo,[a,b] Zeyu Lyu,*[b] Dashuai Sun,[b] Sida Shen,[b] Taixing Tan,[b] Shuai Wei,[a,b] Zhijun Li,[a,b] Pengcheng Luo[a,b] and Hongpeng You ✪ *[a,b,c]

Na₂MgScF₇ (NMSF) was experimentally obtained for the first time by combining hydrothermal and high-temperature solid-state reactions. X-ray powder diffraction (XRD) combined with Rietveld refinement confirms that NMSF is crystallized in the space group *Imma* with the cell parameters $a = 10.40860(18)$, $b = 7.32804(12)$ and $c = 7.52879(11)$ Å, $\alpha = \beta = \gamma = 90°$ and $V = 574.256(24)$ Å^3. Through doping with Tb^{3+} or Eu^{3+} ions, downshifting yellow-green or red emission could be achieved in NMSF-based phosphors, respectively. Upconversion emission could also be designed by doping with $Yb^{3+}–Er^{3+}$, $Yb^{3+}–Tm^{3+}$, $Yb^{3+}–Ho^{3+}$ or Er^{3+}. Moreover, the NMSF:Er^{3+} phosphor exhibited green upconversion emission upon excitation at 980 nm, and it exhibited red emission upon excitation at 1532 nm. Finally, recognizable patterns were obtained under excitation at 254, 365 and 980 nm, indicating that the as-prepared phosphors can be applied to multicolor anti-counterfeiting. Moreover, our synthesis strategy opens up new avenues for the synthesis of novel fluorides.

1 Introduction

Counterfeit and shoddy products seriously interfere with the development of market economies. Various anti-counterfeiting technologies have emerged, such as watermarks,[1] bar codes[2] and optical anti-counterfeiting.[3,4] Among them, optical anti-counterfeiting technology has many advantages, including easy fabrication, hard to imitate, good stability and high recognition rates, and it can be combined with other anti-counterfeiting technologies to achieve higher security levels. The main challenge of optical anti-counterfeiting technology is to develop multicolor luminous materials with multicolor emissions.[5–7]

Lanthanide ions possess rich electronic energy levels from their 4f electrons, which endow them with unique luminescence properties, such as narrow spectral bands, large Stokes shifts, long lifetimes and high photochemical stability. There are two main emission modes in Ln^{3+}-doped luminescent materials: downshifting (DS) and upconversion (UC),[8] where

aSchool of Chemistry and Chemical Engineering, Nanchang University, Nanchang 330031, P.R. China. E-mail: hpyou@ciac.ac.cn
bGanjiang Innovation Academy, Chinese Academy of Sciences, Ganzhou 341000, P. R. China. E-mail: zylyu@gia.cas.cn
cState Key Laboratory of Rare Earth Resource Utilization, Changchun Institute of Applied Chemistry, Chinese Academy of Sciences, Changchun 130022, P. R. China
†Electronic supplementary information (ESI) available. See DOI: https://doi.org/10.1039/d3dt00746d

DS is the process of the emission of a lower energy photon after absorption of a higher energy photon, also known as Stokes emission.[5] Tb^{3+} and Eu^{3+} ions are two familiar ions for their DS luminescence. The Tb^{3+} ion is known for its strong green emission with a transition from the $^5D_4$ to $^7F_5$ energy level.[9–13] The Eu^{3+} ion usually emits strong red light, and the emission wavelength range is 550–650 nm, corresponding to the transition of the $^5D_0$ to ^7F_n energy level.[14–16] On the basis of the ladder-like energy levels, some of the lanthanide ions can realize UC emission, which can convert two or more lower-energy photons into one higher-energy photon. Typically, three ion pairs, $Yb^{3+}–Er^{3+}$, $Yb^{3+}–Tm^{3+}$ and $Yb^{3+}–Ho^{3+}$, have attracted great attention for their efficient UC emissions through the energy transfer upconversion (ETU) mechanism, in which the sensitizer (Yb^{3+}) absorbs lower energy photons and then donates energy to the activator (Er^{3+}, Tm^{3+} or Ho^{3+}) sequentially.[17–20] In addition, the Er^{3+} ion can realize UC emission through the mechanism of excited state absorption (ESA), in which Er^{3+} in the excited state absorbs another low-energy photon (such as 980 and 1530 nm) and then emits a high-energy photon.[21,22] The UC emissions from lanthanide ions exhibit great tunability in colors from the aspects of energy transfer and remote manipulation.[23] Therefore, lanthanide ions are highly suitable for the design of luminescent materials with multicolor emissions for high-security anti-counterfeiting.

Generally, lanthanide ions need to be doped into a host lattice to obtain luminescence. Therefore, a suitable host

material is of critical importance to design a luminescent material.[24–26] Host crystals can be divided into fluorides, oxides, sulfides, and so on. Among them, fluorides are considered to be excellent hosts for UC luminescence owing to their low phonon energy, which alleviates the non-radiative relaxation to achieve high UC efficiency.[27] Therefore, fluoride hosts for UC have supported their application in multiplexing,[28,29] orientation sensors,[30,31] micro-lasers,[32,33] STED,[34,35] and so on. However, the variety of fluoride phosphors is relatively small compared with oxide systems, and this limits the exploration of novel functional materials. This may be due to the fact that fluorides are mainly synthesized by solution methods, through which it is more difficult to obtain products of specified compositions because of the different solubilities of different fluorides.

Herein, the combination of hydrothermal and high-temperature solid-state reactions enables the synthesis of a quad-element fluoride, Na_2MgScF_7(NMSF). NMSF crystallizes in the orthorhombic crystal system, and the space group is *Imma*. Importantly, the Sc^{3+} site can be doped with luminescent lanthanide ions to obtain luminescent materials. Under excitation at 365 nm, NMSF:Tb^{3+} and NMSF:Eu^{3+} can emit efficient yellow-green light and red light, respectively. With the doping of Yb^{3+} and Er^{3+}/Ho^{3+}/Tm^{3+} ions, typical UC emissions can be realized through the ETU process. Moreover, the UC of NMSF:Er^{3+} through the ESA process exhibits tunable emissions from green to red by changing the excitation from 980 to 1532 nm. These doped NMSF phosphors show great potential in multicolor anticounterfeiting applications.

2 Experimental section

2.1 Materials

The starting materials of Sc_2O_3 (99.99%), NH_4F (98.0%), NH_4HF_2 (AR), Er_2O_3 (99.99%), MgF_2 (99%), Tb_4O_7 (99.99%), Eu_2O_3 (99.99%), Yb_2O_3 (99.99%), Tm_2O_3 (99.99%), Ho_2O_3 (99.99%), NaF (98.0%) and HF (49 wt%) were commercially purchased and used without further purification. Sc_2O_3 was purchased from Hunan Rare Earth Metal Materials Research Co., Ltd (China). NH_4F, NH_4HF_2 and Er_2O_3 were supplied by Aladdin Industrial Corporation, while the other chemicals were supplied by Shanghai Titan Scientific Co., Ltd (China).

2.2 Preparation of NMSF phosphors

Synthesis of lanthanide fluorides. LnF_3 compounds (Ln = Yb, Er, Ho, Tm, Tb, Eu,) were prepared by heating the corresponding mixture of lanthanide oxides with NH_4HF_2 at 500 °C for 24 h. The XRD patterns of the corresponding products confirmed the successful preparation of phase-pure lanthanide fluorides (Fig. S1†).

Synthesis of the intermediate $(NH_4)_2NaScF_6$. $(NH_4)_3ScF_6$ was synthesized according to a reported method.[36] $(NH_4)_3ScF_6$ and excess NaF were mixed in a 100 mL beaker, and stirred for 1 h; then, excess NH_4F solution was added and the mixture was stirred for another 1 h. Subsequently, the solution was poured

into a reaction kettle and reacted at 200 °C for 12 h. The obtained sample was washed several times with 95% ethanol and ultrapure water. The Rietveld refinement based on the XRD pattern confirmed the successful preparation of $(NH_4)_2NaScF_6$ (Fig. S2†).[37]

Synthesis of Na_2MgScF_7:Yb^{3+},Er^{3+}. NaF, MgF_2, YbF_3, ErF_3 and $(NH_4)_2NaScF_6$ were weighed according to the stoichiometric ratio and then ground in an agate mortar for 20 min; then, the mixture was heated at 830 °C under a nitrogen atmosphere for 5 h. The resulting samples were fully ground and washed with HF solution to remove Na_3ScF_6 impurity.

2.3 Characterization

The XRD patterns of the as-synthesized phosphors were recorded through a RigakuD/max-RA X-ray diffractometer with Cu Kα radiation (λ = 1.5406 Å) in the 2θ range from 10 to 80°. The General Structural Analysis System (GSAS) program was used to perform the Rietveld refinement of the XRD patterns with optimized scale factor, zero offset, background and cell parameters. The particle morphology was obtained by high-resolution field emission scanning electron microscopy (SEM) with the use of a JSM-IT800 instrument (Nippon Electron Co., Japan) The photoluminescence excitation (PLE) and emission (PL) spectra were analyzed on a Hitachi F-7100 spectrophotometer with external 980 or 1532 nm lasers as the excitation sources for the UC spectra.

3 Results and discussion

3.1 Phase identification, structure, and morphology

The synthesis of multi-elemental oxides is usually based on the simple calcination of commercial precursors. In contrast, the calcination of NaF, MgF_2 and ScF_3 cannot yield the target material, but can produce Na_3ScF_6 and $NaMgF_3$ (Fig. S3†). The products of the direct precipitation of Na^+, Mg^{2+}, Sc^{3+} and F^- in solution also produce these two fluorides (Fig. S3†). The synthesis of NMSF is based on a combination of hydrothermal and high-temperature solid-state reactions, where $(NH_4)_2NaScF_6$ is used as an intermediate in the hydrothermal synthesis (Fig. 1a). The phase purity of the as-prepared series of NMSF systems was characterized by XRD analysis. Fig. 1b shows the XRD patterns of the prepared NMSF and NMSF:Ln^{3+} (Ln = Tb, Eu, Yb–Er) samples. All patterns are well matched with the standard PDF card (PDF#26-0965),[38] indicating the successful synthesis of phase-pure NMSF.

The Rietveld refinements of NMSF and NMSF:5%Tb^{3+} were carried out using the GSAS program, and some of the crystal data are summarized in Table S1.† Fig. 1c and d exhibit the experimental and calculated results of the Rietveld refinements for two samples, showing that the dopant ions are successfully incorporated into the NMSF crystal host without any phase impurities. The SEM image of NMSF:5%Tb^{3+} is shown in Fig. 1e. The shapes of the NMSF:5%Tb^{3+} particles are irregular with an average diameter of ~3.0 μm. Fig. 1f shows the crystal structure of NMSF, which is crystallized in the space
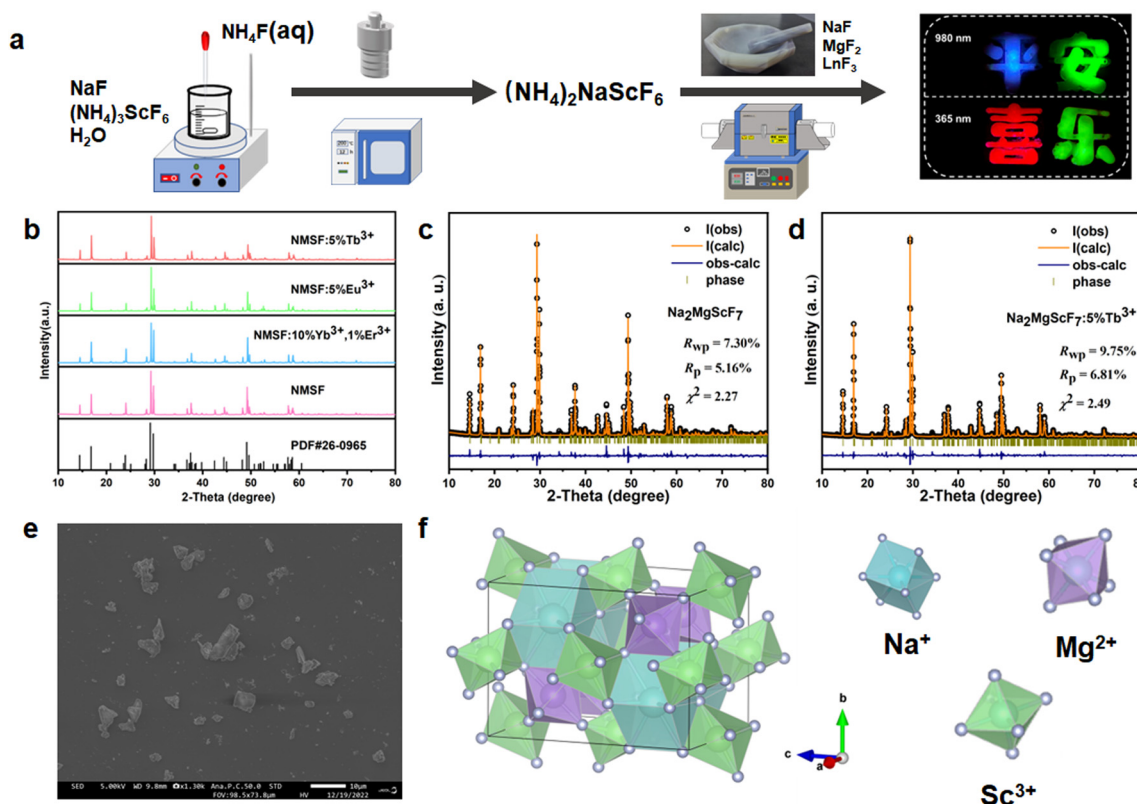
Fig. 1 (a) Synthesis routine for NMSF; (b) XRD patterns of the NMSF and NMSF:Ln^{3+} (Ln = Tb, Eu, Yb−Er) samples; (c and d) Rietveld refinement of the XRD patterns of NMSF and NMSF:5%Tb^{3+}; (e) SEM image of NMSF:5%Tb^{3+}; and (f) crystal structure of NMSF and the coordination environment of Na$^+$, Mg^{2+} and Sc^{3+}.

group *Imma*. In this structure, Na$^+$ is bonded with eight F$^-$ in a twisted body-centered cubic geometry, including four shorter bonds and four longer bonds. In addition, Mg^{2+} and Sc^{3+} are both bonded with six F$^-$ to form the MgF$_6$ and ScF$_6$ octahedra.

3.2 DS luminescence properties

Fig. 2a shows the PL and PLE spectra of NMSF:5%Tb^{3+} at room temperature. The PLE spectra of NMSF:5%Tb^{3+} monitored at 543 nm consist of a strong band from 200 to 300 nm with a maximum at 219 nm, which can be attribu-

ted to the 4f^8 → 4f^{7}5d^1 transition of the Tb^{3+} ions and the bands in the range of 300–400 nm are derived from the 4f → 4f transitions of the Tb^{3+} ions.[9] Under excitation at 254 nm, the PL spectrum of the Tb^{3+} ions consists of four emission bands centered at 488, 544, 587 and 623 nm originating from the transitions of the Tb^{3+} ions from the $^5D_4$ excited state to the ^7F_J (J = 6, 5, 4, 3) ground states.[39,40] The CIE chromaticity coordinates of the emissions are (0.2744, 0.4475), indicating that the emission color is yellow-green. In addition, the downshifting emissions from the Eu^{3+} ions in NMSF are investigated (Fig. 2b). Under the monitoring of the emission at 594 nm, the PLE spectra are composed of many sharp peaks with a band maximum at 393 nm, and the peaks at 319, 361, 382, 393, 416, 465 and 526 nm correspond to the $^7F_0 \rightarrow {}^5H_6$, $^7F_0 \rightarrow {}^5D_4$, $^7F_0 \rightarrow {}^5G_2$, $^7F_0 \rightarrow {}^5L_6$, $^7F_0 \rightarrow {}^5D_3$, $^7F_0 \rightarrow {}^5D_2$ and $^7F_0 \rightarrow {}^5D_1$ transitions, respectively.[41,42] The PL spectra exhibit typical red emission, mainly originating from the $^5D_0 \rightarrow {}^7F_1$(593 nm), $^5D_0 \rightarrow {}^7F_2$(617 nm), $^5D_0 \rightarrow {}^7F_3$ (655 nm) and $^5D_0 \rightarrow {}^7F_4$ (708 nm) transitions of the Eu^{3+} ions.[43–45] The CIE chromaticity coordinates of the Eu^{3+} ion emission are (0.5086, 0.3334) in the orange-red region. It is worth mentioning that Fig. S4† shows the PL spectra of NMSF phosphors with different doping contents of Tb^{3+} or Eu^{3+}. The optimal doping concentration was 7% for NMSF:Tb^{3+} and 5% for NMSF:Eu^{3+}.
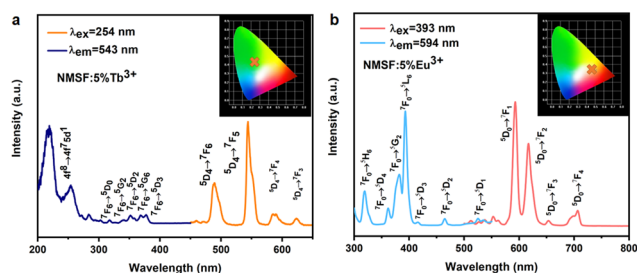
Fig. 2 (a) PL and PLE spectra of NMSF:5%Tb^{3+}; the inset panel is the CIE chromaticity coordinates of the emission from NMSF:5%Tb^{3+}. (b) PL and PLE spectra of NMSF:5%Eu^{3+}; the inset panel is the CIE chromaticity coordinates of the emission from NMSF:5%Eu^{3+}.

3.3 UC luminescence properties

The UC emission can be produced through doping with specific lanthanide ions, such as Yb^{3+}–Er^{3+}, Yb^{3+}–Tm^{3+}, Yb^{3+}–Ho^{3+} and Er^{3+}. Fig. 3a shows the typical UC spectra of NMSF:10%Yb^{3+},1%Er^{3+} recorded under 980 nm laser excitation with different powers. Three different emission bands in the visible range were observed. To investigate the UC mechanism, the PL intensity dependence on the excitation power density of NMSF:10%Yb^{3+},1%Er^{3+} is plotted in Fig. 3b. In principle, the output UC emission intensity is dependent on the infrared pump power according to the following formula:

$$I_{uc} \propto (I_{IR})^n$$

where n is the number of photons that need to be absorbed for each UC photon emitted.[46,47] The linear fits of $\log(I_{uc})$ and $\log(I_{IR})$ result in fitted slopes of 1.77 and 1.61 for the green and red emissions, respectively. The results indicate that both emissions originate from a two-photon ETU process. Therefore, the two green emission bands peaking at 523 and 545 nm and a red emission band peaking at 650 nm are due to the $^2H_{11/2} \rightarrow {}^4I_{15/2}$, $^4S_{3/2} \rightarrow {}^4I_{15/2}$ and $^4F_{9/2} \rightarrow {}^4I_{15/2}$ transitions, respectively (Fig. 3c).[4,48,49]

Furthermore, the UC emissions from the Yb^{3+}–Tm^{3+} and Yb^{3+}–Ho^{3+} pairs in the NMSF matrix were also explored. Fig. 4a shows the UC spectra of NMSF:10%Yb^{3+},1%Ho^{3+} under 980 nm laser excitation. One can see three emission bands (Fig. 4a). The relationships between the emission intensity and the excitation power were investigated, and the slopes of the linear fitting of the $\log(I_{uc})$ versus $\log(I_{IR})$ are all ~1.7 (Fig. 4b), denoting that the three emission bands are from a two-photon ETU process. Therefore, the emission bands peaking at 545, 661 and 750 nm correspond to the $^5F_4,{}^5S_2 \rightarrow {}^5I_8$, $^5F_5 \rightarrow {}^5I_8$ and $^5F_4,{}^5S_2 \rightarrow {}^5I_7$ transitions, respectively (Fig. 4c).[50,51] For the NMSF:10%Yb^{3+},2%Tm^{3+} sample, the UC spectrum consists of a blue emission band at 443–512 nm, and a strong red emission band at 640–710 nm. The relationship between the excitation power and the emission intensity was determined as

mentioned above, and the slopes of the obtained blue and red emission bands are 2.26 and 2.49, respectively. These results indicate that the emissions are caused by a three-photon ETU process. Therefore, the blue and red emissions from the Tm^{3+} ions are attributed to the $^1G_4 \rightarrow {}^3H_6$ and $^1G_4 \rightarrow {}^3F_4$ transitions, respectively.[20]

In contrast to the above three ion pairs, which realize UC emission through the ETU process, Er^{3+} can produce UC emission through the ESA process.[21,52–54] Herein, Er^{3+}-doped NMSF was synthesized and its UC emissions under the excitation of 980 and 1532 nm lasers were investigated. Strikingly, the UC emissions from the Er^{3+} ions can be tuned with different excitation wavelengths (Fig. 5a and b). Under excitation at 980 nm, the UC spectrum consists of green and red emissions with a similar intensity. However, the red emission is significantly stronger than the green one when the excitation is with a 1532 nm laser. Therefore, the UC emission under the 980 nm excitation is close to the color of yellow-green, while that under 1532 nm excitation is close the color of yellow-red (Fig. 5b). The emission selectivity comes from the different UC processes.

Under excitation at 980 nm, the electrons of the Er^{3+} ions are excited from the ground state $^4I_{15/2}$ to $^4I_{11/2}$ by the ground state absorption (GSA), and the electrons in the $^4I_{11/2}$ level are either further excited to the $^4F_{7/2}$ level or relax to the $^4I_{13/2}$ level. The electrons in the $^4F_{7/2}$ level relax to the $^4S_{3/2}$ and $^2H_{11/2}$ levels, which give the green emission. The electrons in the $^4I_{13/2}$ level can be further excited to the $^4F_{9/2}$ level and then give the red emission (Fig. 5c). Thus, the relaxation between the $^4I_{11/2}$ and $^4I_{13/2}$ levels decreases the green–red ratio. On the other hand, the electrons in the ground state of the Er^{3+} ions are firstly excited to the $^4I_{9/2}$ level by absorbing two 1532 nm photons in succession under excitation at 1532 nm. The electrons in the $^4I_{9/2}$ level are either further excited to the $^4S_{3/2}$ and $^2H_{11/2}$ levels, resulting in green emission, or relax to the $^4I_{11/2}$ level and then excited to the $^4F_{9/2}$ level, resulting in the red emission (Fig. 5d). In the case of 1532 nm excitation, the relaxation between the $^4I_{9/2}$ and $^4I_{11/2}$ levels decreases the green–red ratio. In comparison, the relaxation between the $^4I_{9/2}$ and $^4I_{11/2}$

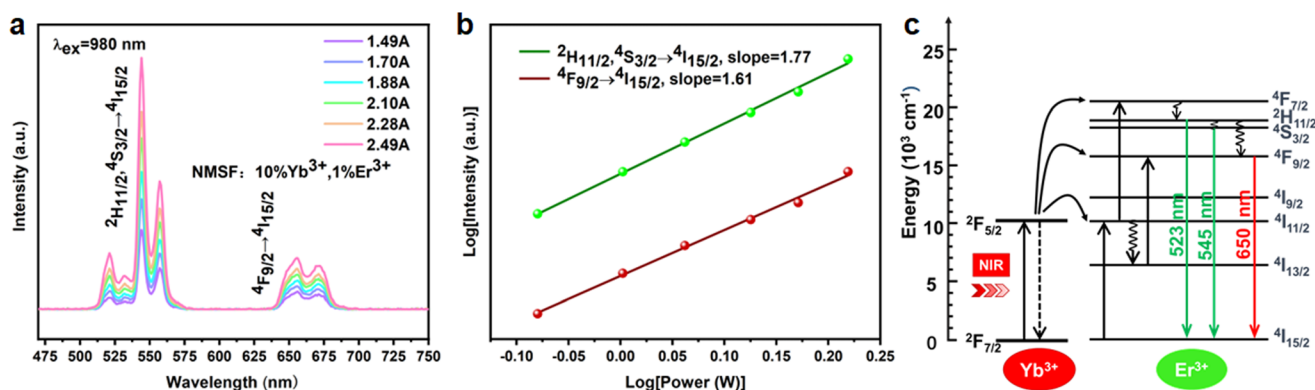**Fig. 3** (a) UC spectra of NMSF:10%Yb^{3+},1%Er^{3+} at 980 nm laser excitation with different powers. (b) Plots of logarithm intensity of the UC emission *versus* logarithm pumped power. (c) UC mechanism of NMSF:10%Yb^{3+},1%Er^{3+} under the excitation of 980 nm.

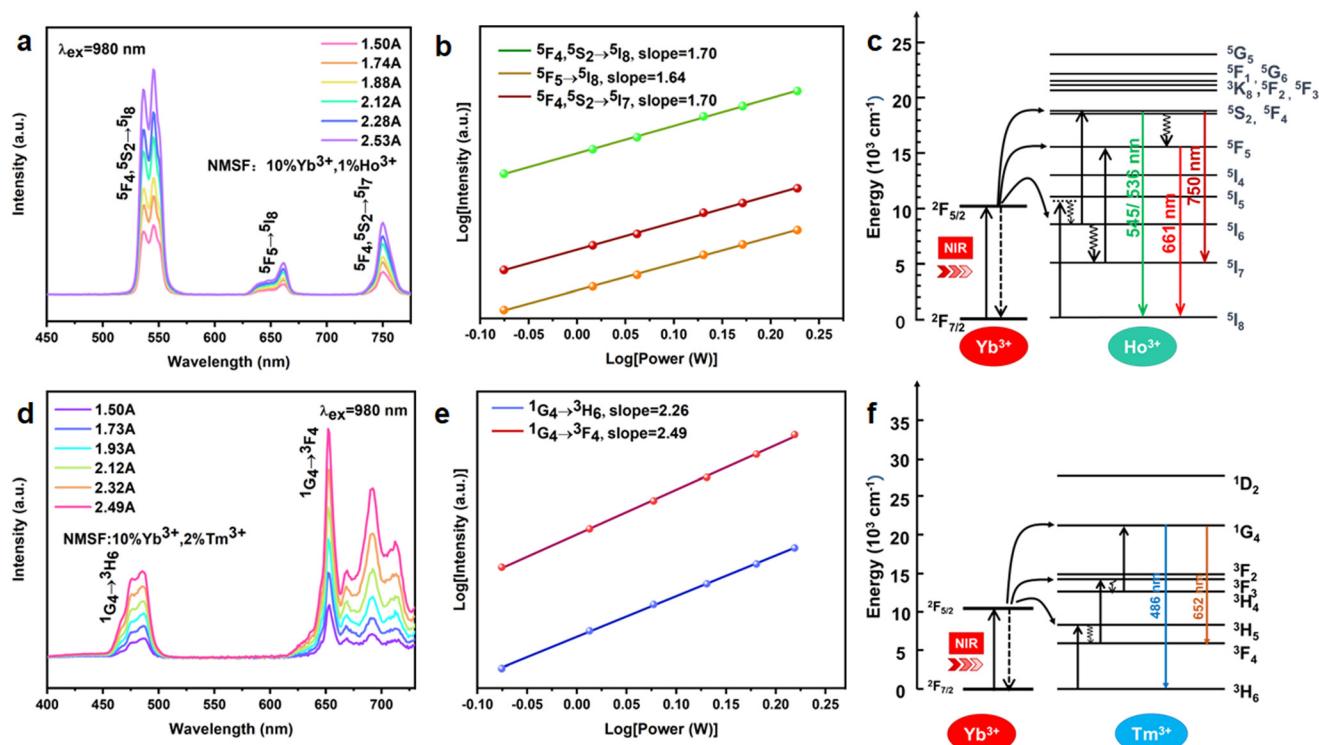**Fig. 4** (a and d) UC spectra of NMSF:10%Yb^{3+},1%Ho^{3+} and NMSF:10%Yb^{3+},2%Tm^{3+} under 980 nm laser excitation with different powers. (b and e) Plots of logarithm intensity of the UC emission *versus* logarithm pumped power. (c and f) UC mechanism of NMSF:10%Yb^{3+},1%Ho^{3+} and NMSF:10% Yb^{3+},2%Tm^{3+} under excitation at 980 nm.
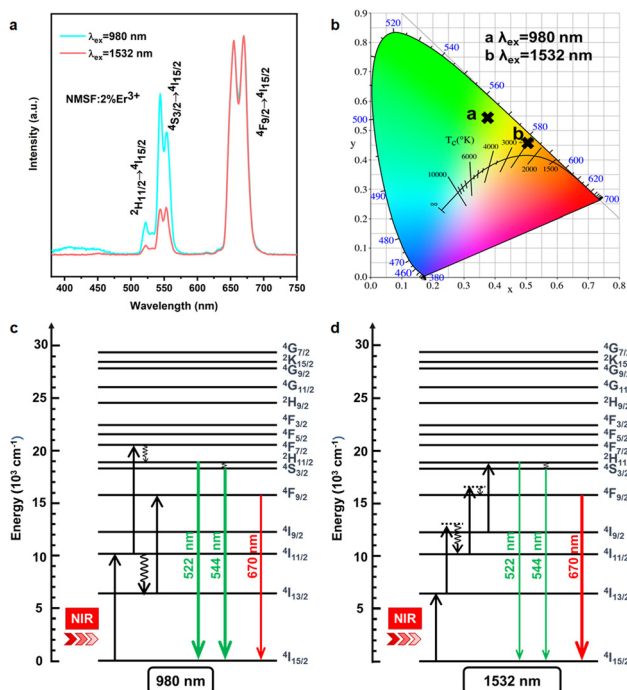

Fig. 5 (a) UC spectra of NMSF:2%Er^{3+} under the excitation of 980 and 1532 nm laser. (b) CIE chromaticity coordinates of NMSF:2%Er^{3+} at 980 and 1532 nm excitation. (c) UC mechanism of NMSF:2%Er^{3+} under excitation at 980 nm. (d) UC mechanism of NMSF:2%Er^{3+} under excitation at 1532 nm.

levels should be easier than that between the $^4I_{11/2}$ and $^4I_{13/2}$ levels because of the smaller energy gaps ($\sim$2000 cm^{-1} *versus* $\sim$3900 cm^{-1}). Therefore, the green–red ratio under the 1532 nm excitation is smaller than that under the 980 nm excitation.

3.4 Anti-counterfeiting applications

On the basis of the doped NMSF phosphors, multicolor anti-counterfeiting can be designed, as shown in Fig. 6. NMSF:10% Yb^{3+},1%Tm^{3+}, NMSF:10%Yb^{3+},1%Er^{3+}, NMSF:5%Eu^{3+} and NMSF:5%Tb^{3+} were mixed with glue in the ratio of 1 : 10, and
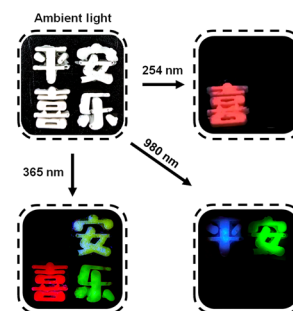

Fig. 6 Multicolor anti-counterfeiting with doped NMSF phosphors. The word "平" contains NMSF:10%Yb^{3+},1%Tm^{3+}; the word "安" contains NMSF:10%Yb^{3+},1%Er^{3+}; the word "喜" contains NMSF:5%Eu^{3+}; and the word "乐" contains NMSF:5%Tb^{3+}.
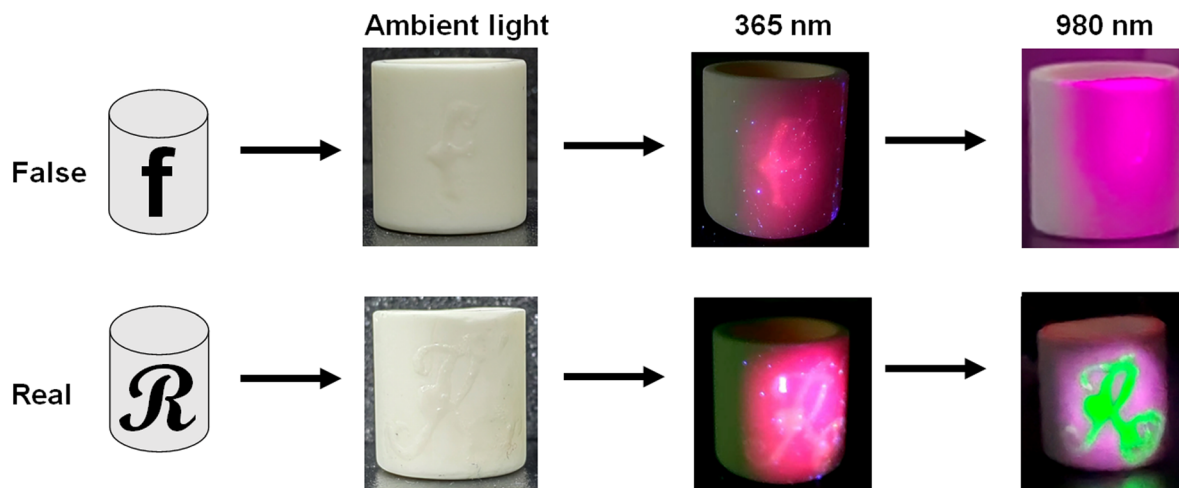
Fig. 7 Multicolor anti-counterfeiting with doped NMSF phosphors to distinguish crucibles.

then introduced into a silicone mold, which was placed in an 80 °C oven for 24 h to cure. After that, four characters were obtained. Under the illumination of a 254 nm UV lamp, only the character "喜" emits weak red light. Under the irradiation of a 365 nm UV lamp, the character "安" emits weak green light, while the characters "喜" and "乐" emit strong red and yellow-green light, respectively. Under the illumination of a 980 nm laser, the character "平" emits blue light, while the character "安" emits green light. The highly distinguishable patterns under different excitation denote the potential application in multicolor anti-counterfeiting. Moreover, compared with some other reported luminescent materials capable of both DS and UC emissions for anti-counterfeiting,[55–58] the presented NMSF-based phosphors should be more efficient in the UC emissions, because of the low phonon energy and efficient ETU processes, and four ionic combinations of UC have been realized in NMSF.

To further demonstrate the application in anti-counterfeiting, a practical situation was investigated, in which the doped NMSF phosphors were applied to distinguish crucibles. As shown in Fig. 7, a crucible was labeled with the letter "f", which contained NMSF:5%Eu^{3+}, and another crucible was labeled with the letter "R", which contained NMSF:5%Eu^{3+} and NMSF:10%Yb^{3+},1%Er^{3+}. Under the illumination of a 365 nm UV lamp, both the letters "f" and "R" turn red, because of the red emission from the Eu^{3+} ions. However, the emission from the crucible interfered with the readout of the letters. In comparison, the letter "R" color turns well-recognized green under the illumination of a 980 nm laser because of the UC emission from the Yb^{3+}–Er^{3+} ions. It is worth mentioning that purple light around the "R" is attributed to the scattered 980 nm laser, which appears purple in the camera, but is invisible to human eyes. This observation indicates that the integration of DS and UC emission offers more reliable anti-counterfeiting.

4 Conclusions

In summary, we synthesized a novel fluoride phosphor NMSF: Ln^{3+} by the combination of hydrothermal and high-temperature solid-state reactions. The prepared phosphors have an average particle size of ~3.0 μm. The DS emissions of yellow-green light and red light were observed through doping the Tb^{3+} and Eu^{3+} ions, respectively. In addition, the UC emissions from the ETU process of the Yb^{3+}–Er^{3+}, Yb^{3+}–Tm^{3+} and Yb^{3+}–Ho^{3+} ion pairs were achieved. Moreover, the UC emission from the NMSF:Er^{3+} phosphor shows different selectivities under excitation at 980 and 1532 nm, which is attributed to the different relaxation of intermediate states. Finally, distinguishable patterns at different excitation wavelengths were obtained using the as-prepared Ln^{3+}-doped NMSF, indicating that the obtained NMSF-based phosphor can be used for anti-counterfeiting applications. The recognizable patterns were obtained at 254, 365 and 980 nm, indicating that the prepared phosphors can be applied to multicolor anti-counterfeiting. Moreover, our work would provide guidance for the synthesis of novel fluorides.

Author contributions

Data curation: Chengyu Zhuo; formal analysis: Zeyu Lyu and Dashuai Sun; investigation: Pengcheng Luo, Shuai Wei and Zhijun Li; methodology: Sida Shen and Taixing Tan; writing—original draft: Chengyu Zhuo; writing—review and editing: Zeyu Lyu and Hongpeng You. All authors have read and agreed to the published version of the manuscript.

Conflicts of interest

There are no conflicts to declare.

Acknowledgements

References

1 R. Xie, C. Hon, S. Zhu and D. Tao, *Neurocomputing*, 2015, **167**, 625–635.

2 S. Han, H. Bae, J. Kim, S. Shin, S. Choi, S. Lee, S. Kwon and W. Park, *Adv. Mater.*, 2012, **24**, 5924–5929.

3 H. Suo, Q. Zhu, X. Zhang, B. Chen, J. Chen and F. Wang, *Mater. Today Phys.*, 2021, **21**, 100520.

4 Z. J. Li, Z. Y. Lyu, D. S. Sun, S. D. Shen and H. P. You, *Mater. Today Chem.*, 2022, **26**, 101116.

5 X. Chen, W. J. Yao, Q. Wang and W. Wu, *Adv. Opt. Mater.*, 2019, **8**, 1901209.

6 H. Huang, J. Chen, Y. Liu, J. Lin, S. Wang, F. Huang and D. Chen, *Small*, 2020, **16**, 2000708.

7 Z. B. Wang, L. W. Yang, Z. B. Wang, J. J. Cao, C. H. Ma, M. J. Zhang and W. S. Liu, *Dalton Trans.*, 2023, **52**, 2145–2156.

8 L. Mariscal-Becerra, V. M. Velázquez-Aguilar, M. C. Flores-Jiménez, D. Acosta-Najarro, V. Torres-Zúñiga, R. Váquez-Arreguín, E. F. Huerta, H. Félix-Quintero, C. Falcony-Guajardo and S. H. Murrieta, *J. Alloys Compd.*, 2020, **846**, 156295.

9 T. X. Shi, F. Liu, J. H. Zhang and X. J. Wang, *J. Mater. Chem. C*, 2022, **10**, 15353–15357.

10 Y. Wang, P. Darapaneni, O. Kizilkaya and J. A. Dorman, *Inorg. Chem.*, 2020, **59**, 2358–2366.

11 X. G. Zuo, Y. Wang, L. Wei, X. S. Lv, Y. B. Fu, J. Li, Z. Y. Hang, X. P. Wang, B. Liu and Y. G. Yang, *CrystEngComm*, 2021, **23**, 4194–4204.

12 Z. Lu, D. S. Sun, Z. Y. Lyu, S. D. Shen, L. X. Wang, J. H. Wang, H. W. Zhao and H. P. You, *J. Am. Ceram. Soc.*, 2022, **106**, 1182–1193.

13 V. V. Atuchin, A. S. Aleksandrovsky, O. D. Chimitova, A. S. Krylov, M. S. Molokeev, B. G. Bazarov, J. G. Bazarova and Z. G. Xia, *Opt. Mater.*, 2014, **36**, 1631–1635.

14 P. Solarz, M. Sobczyk, E. Beregi, R. Lisiecki, K. Lengyel, L. Kovács and W. Ryba-Romanowski, *J. Lumin.*, 2023, **257**, 119717.

15 B. Yu, J. L. Chen, M. H. Sun, N. M. Chen, Y. C. Li and Y. J. Wang, *Dalton Trans.*, 2022, **51**, 2932–2942.

16 P. L. Shi, Z. G. Xia, M. S. Molokeev and V. V. Atuchin, *Dalton Trans.*, 2014, **43**, 9669–9676.

17 Y. L. Zhang, P. Lv and Z. K. Qin, *J. Nanomater.*, 2019, **2019**, 1–7.

18 F. Ayachi, K. Saidi, W. Chaabani and M. Dammak, *J. Lumin.*, 2021, **240**, 118451.

19 J. Zhang, J. J. Chen and Y. N. Zhang, *Inorg. Chem. Front.*, 2020, **7**, 4892–4901.

20 J. Zhang, X. M. Jiang and Z. H. Hua, *Ind. Eng. Chem. Res.*, 2018, **57**, 7507–7515.

21 L. Liu, S. Wang, B. Zhao, P. Pei, Y. Fan, X. Li and F. Zhang, *Angew. Chem., Int. Ed.*, 2018, **57**, 7518–7522.

22 X. Du, X. Wang, L. Meng, Y. Bu and X. Yan, *Nanoscale Res. Lett.*, 2017, **12**, 163.

23 J. S. Zhang, Y. Z. Zhang, J. Tao and Y. N. Zhu, *Mater. Res. Express*, 2018, **5**, 046201.

24 H. Ju, X. Deng, Z. Weng, Q. Wu, B. Wang, Y. Ma and H. Wang, *Ceram. Int.*, 2016, **42**, 6846–6849.

25 B. Zhao, D. Y. Shen, J. Yang, S. S. Hu, X. J. Zhou and J. F. Tang, *J. Mater. Chem. C*, 2017, **5**, 3264–3275.

26 P. Zhang, J. Ke, D. Tu, J. Li, Y. Pei, L. Wang, X. Shang, T. Guan, S. Lu, Z. Chen and X. Chen, *Angew. Chem., Int. Ed.*, 2022, **61**, 2–10.

27 R. Naccache, Q. Yu and J. A. Capobianco, *Adv. Opt. Mater.*, 2015, **3**, 482–509.

28 Z. Y. Lyu, H. Dong, X. F. Yang, L. Huang, Y. J. Xu, K. Wu, L. D. Sun and C. H. Yan, *JACS Au*, 2023, **3**, 860–867.

29 H. Dong, L. D. Sun, W. Feng, Y. Gu, F. Li and C. H. Yan, *ACS Nano*, 2017, **11**, 3289–3297.

30 Z. Y. Lyu, H. Dong, X. F. Yang, L. D. Sun and C. H. Yan, *J. Phys. Chem. Lett.*, 2021, **12**, 11288–11294.

31 S. Q. Wei, X. Y. Shang, P. Huang, W. Zheng, E. Ma, J. Xu, M. Zhang, D.T Tu and X. Y. Chen, *Sci. China Mater.*, 2021, **65**, 220–228.

32 X. F. Yang, Z. Y. Lyu, H. Dong, L. D. Sun and C. H. Yan, *Small*, 2021, **17**, 2103140.

33 A. Fernandez-Bravo, K. Yao, E. S. Barnard, N. J. Borys, E. S. Levy, B. Tian, C. A. Tajon, L. Moretti, M. V. Altoe, S. Aloni, K. Beketayev, F. Scotognella, B. E. Cohen, E. M. Chan and P. J. Schuck, *Nat. Nanotechnol.*, 2018, **13**, 572–577.

34 Y. Liu, Y. Lu, X. Yang, X. Zheng, S. Wen, F. Wang, X. Vidal, J. Zhao, D. Liu, Z. Zhou, C. Ma, J. Zhou, J. A. Piper, P. Xi and D. Jin, *Nature*, 2017, **543**, 229–233.

35 Q. Zhan, H. Liu, B. Wang, Q. Wu, R. Pu, C. Zhou, B. Huang, X. Peng, H. Agren and S. He, *Nat. Commun.*, 2017, **8**, 1058.

36 F. Q. He, E. H. Song, Y. Y. Zhou, H. Ming, Z. T. Chen, J. C. Wu, P. S. Shao, X. F. Yang, Z. G. Xia and Q. Y. Zhang, *Adv. Funct. Mater.*, 2021, **31**, 2103743.

37 J. Chassain, *C. R. Seances Acad. Sci., Ser. C*, 1971, **272**, 209.

38 J. Chassain, *C. R. Seances Acad. Sci., Ser. C*, 1969, **268**, 2188.

39 H. Dong, L. D. Sun, Y. F. Wang, J. W. Xiao, D. T. Tu, X. Y. Chen and C. H. Yan, *J. Mater. Chem. C*, 2016, **4**, 4186–4192.

40 X. G. Zhang, Z. C. Wu, F. W. Mo, N. Li, Z. Y. Guo and Z. P. Zhu, *Dyes Pigm.*, 2017, **145**, 476–485.

41 D. Shen, B. Zhao, S. Yang, S. Hu, J. Tang, X. Zhou and J. Yang, *J. Mater. Sci.*, 2017, **52**, 13868–13878.

42 V. V. Atuchin, A. S. Aleksandrovsky, O. D. Chimitova, T. A. Gavrilova, A. S. Krylov, M. S. Molokeev,

A. S. Oreshonkov, B. G. Bazarov and J. G. Bazarova, *J. Phys. Chem. C*, 2014, **118**, 15404–15411.

43 D. Yang, L. B. Liao, Q. F. Guo, L. J. Wang, L. F. Mei, H. K. Liu and T. S. Zhou, *J. Lumin.*, 2018, **203**, 391–395.

44 N. Yang, Z. W. Zhang, L. Y. Zou, J. Chen, H. Y. Ni, P. Chen, J. X. Shi and Y. X. Tong, *Inorg. Chem. Front.*, 2022, 6358–6368.

45 X. X. Han, E. H. Song, W. B. Chen, Y. Y. Zhou and Q. Y. Zhang, *J. Mater. Chem. C*, 2020, **8**, 9836–9844.

46 J. Liu, D. Mara and V. R. Deun, *J. Alloys Compd.*, 2018, **737**, 767–773.

47 J. Zhang and F. S. Qian, *Dalton Trans.*, 2020, **49**, 10949–10957.

48 X. Jin, Z. Wang, Y. Wei and Z. Fu, *J. Lumin.*, 2022, **249**, 118937.

49 J. Zhang, J. Wang, J. H. Xie, L. X. Wang and Q. T. Zhang, *J. Mater. Sci.: Mater. Electron.*, 2021, **32**, 20882–20890.

50 Y. Feng, B. Shao, S. Zhao and H. You, *CrystEngComm*, 2018, **20**, 7301–7307.

51 X. M. Fan, J. H. Nie, W. T. Ying, S. Q. Xu, J. M. Gu and S. M. Liu, *Dalton Trans.*, 2021, **50**, 12234–12241.

52 V. Prokop, L. Strizik, J. Oswald, M. Vlcek, L. Benes, S. N. Yannopoulos, B. Frumarova and T. Wagner, *Pure Appl. Chem.*, 2019, **91**, 1757–1767.

53 S. F. Gao, T. Z. Chen, M. Y. Hu, S. Xu, Y. Xiong, S. B. Cheng, W. B. Zhang, Y.Q. Wang and W. X. Yang, *Opt. Mater.*, 2019, **98**, 109502.

54 X. Q. Xie, C. Z. Jin, Z. Pan, J. G. Wang, L. Z. Deng, Y. H. Yao, D. L. Qi, Z. R. Sun, J. R. Qiu and S. A. Zhang, *J. Lumin.*, 2023, **255**, 119567.

55 Y. X. Li, C. H. Chen, M. K. Jin, J. M. Xiang, J. J. Tang, Z. Li, W. Chen, J. M. Zheng and C. F. Guo, *Mater. Today Phys.*, 2022, **27**, 100830.

56 Y. X. Li, C. H. Chen, M. K. Jin, J. M. Xiang, J. J. Tang, X. Q. Zhao, J. M. Zheng and C. F. Guo, *J. Lumin.*, 2022, **247**, 118915.

57 Y. J. Wu, X. Q. Zhao, Z. Y. Zhang, J. M. Xiang, H. Suo and C. F. Guo, *Ceram. Int.*, 2021, **4715404**, 15067–15072.

58 M. K. Jin, Y. J. Wu, Z. Y. Zhang, J. M. Xiang and C. F. Guo, *Opt. Laser Technol.*, 2022, **152**, 108144.